ELSEVIER

Contents lists available at ScienceDirect

Additive Manufacturing

journal homepage: www.elsevier.com/locate/addma





Layer-wise engineering of grain orientation (LEGO) in laser powder bed fusion of stainless steel 316L

Karl A. Sofinowski ^{a,1}, Sudharshan Raman ^{a,b,1}, Xiaogang Wang ^a, Bernard Gaskey ^a, Matteo Seita ^{a,b,c,*}

- ^a School of Mechanical and Aerospace Engineering, Nanyang Technological University, Singapore
- ^b Singapore Centre of 3D printing, Nanyang Technological University, Singapore
- ^c School of Material Science and Engineering, Nanyang Technological University, Singapore

ARTICLE INFO

Keywords:
Selective laser melting
Site-specific microstructure control
Stainless steel 316L
Solidification microstructure
Grain orientation engineering
Texture control

ABSTRACT

Additive manufacturing (AM) has opened new possibilities for site-specific microstructure control of metal alloys. In laser powder bed fusion (LPBF) AM, the microstructure can be locally tailored by manipulating the solidification conditions point to point. In this work, we demonstrate this capability by varying the laser scanning angle during LPBF to produce stainless steel samples with controlled crystallographic textures. The resulting microstructures range from strongly textured blocks of arbitrary thickness and shape to gradient crystallographic textures. This strategy paves the way to a new generation of additively manufactured metals with optimized, site-specific properties to suit a wide range of applications.

1. Introduction

One of the defining characteristics of additive manufacturing (AM) is the ability to form material and geometry concurrently at high spatial resolution. This unique capability enables the production of complex, near-net-shape metal parts which can be topology-optimized for improved mechanical performance [1]. It also enables site-specific control over the solidification conditions-and thus the microstructure—within these complex parts. By tuning the process parameters during AM, it is possible to integrate dissimilar microstructures within the same build [2]. This additional degree of freedom opens a new design space for novel components that combine multiple properties [3, 4]. To this end, several studies have explored the capabilities of AM to build spatially varying microstructures for a range of metals. Geiger et al. [5] created blocks of controlled texture by rotating the hatch direction during laser powder bed fusion (LPBF) of Inconel 738. By varying the scanning strategy in electron beam melting (EBM), Dehoff et al. [6] and Helmer et al. [7] were able to switch between columnar and equiaxed grain morphology in Inconel 718. Recently, Todaro et al. [3] achieved similar columnar-to-equiaxed control in both Ti-6Al-4V and Inconel 625 by integrating high intensity ultrasonic fields within the directed energy deposition (DED) process.

In this study, we leverage the site-specific microstructure control capabilities of LPBF to print layers of stainless steel 316L (henceforth 316L) with controlled thickness and grain orientation distribution. We demonstrate the ability to selectively choose the texture perpendicular to the build direction (BD) by simply changing the laser scan angle. Our layer-wise engineering of grain orientation (LEGO²) strategy builds upon the work of Sun et al. [8], who printed single-crystalline-like 316L by maintaining the $\langle 011 \rangle$ orientation along the BD. We show that once the BD orientation is fixed, the remaining rotation angle to drive the formation of a single crystal is determined by the laser scanning angle. Using this approach, we produce LEGO samples with markedly different distributions of texture, which vary either continuously or discretely across the entire build volume. Our results open opportunities for spatial control of texture-dependent properties or to create meta-materials consisting of discrete or gradient regions of texture arranged in arbitrary ways.

2. Methods

In our experiments, we used gas atomized 316L powder with a

https://doi.org/10.1016/j.addma.2020.101809

^{*} Corresponding author at: School of Mechanical and Aerospace Engineering, Nanyang Technological University, Singapore.

¹ Authors contributed equally.

² DISCLAIMER: The acronym "LEGO" presented in this manuscript refers to a metal additive manufacturing method and is not affiliated in any way, shape, or form to Lego System A/S (trade name: The Lego Group) or its associates.

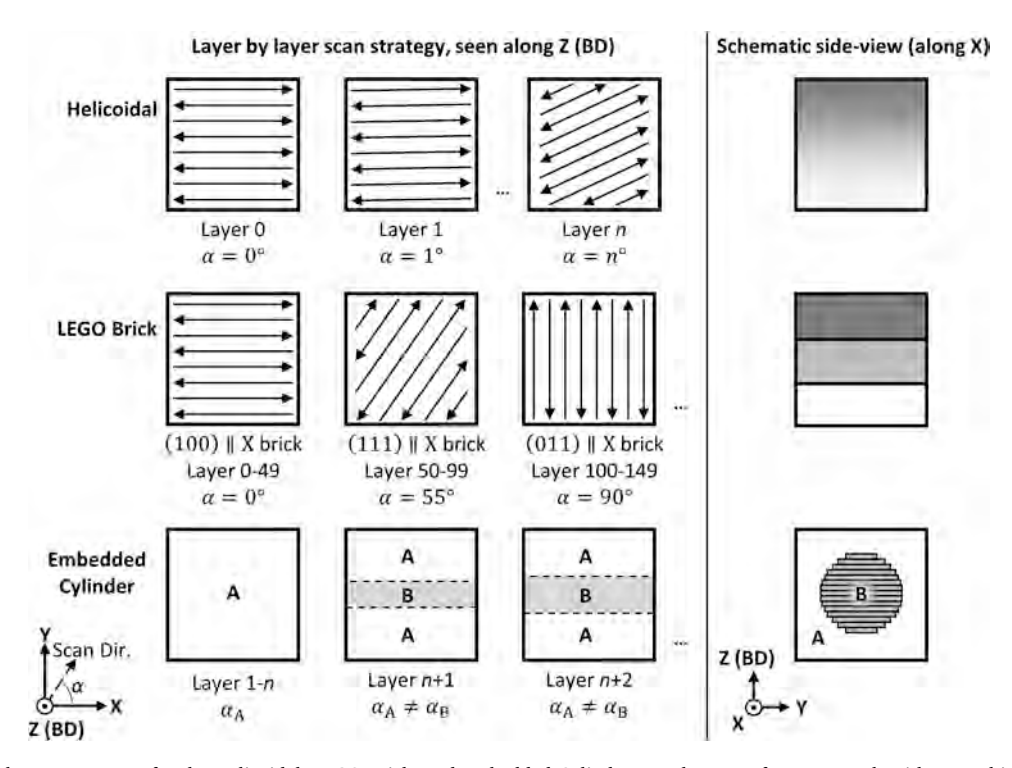


Fig. 1. Schematic of the scan strategy for the Helicoidal, LEGO Brick, and Embedded Cylinder samples, seen from BD, each with a graphic representing the site-specific texture formed perpendicular to BD.

particle size distribution of 20–53 $\mu m.$ The powders had a nominal chemical composition of: 16–18% Cr, 10–14% Ni, 2–3% Mo, < 0.03% C, < 1% Si, < 2% Mn, < 0.045% P, < 0.03% S, < 0.1%N, and Fe balance. We produced cubic samples on top of a 316L build plate under argon atmosphere using an SLM 500 (SLM Solutions, Germany) equipped with a 400-Watt IPG fiber laser. The laser has a Gaussian beam profile with a spot size of 80 $\mu m.$ We set laser power to 240 W, laser scan speed to 600 mm/s, hatch spacing to 100 μm , and layer thickness to 40 μm .

All samples were printed with a bi-directional "serpentine" scan strategy for each layer. To control grain orientation along the normal to BD (i.e. in the X-Y plane), we varied the laser scan angle, α , during LPBF of the LEGO samples. Using this approach, we produced three sets of LEGO samples: the Helicoidal, LEGO Brick, and Embedded Cylinder samples. In the Helicoidal sample, we varied α by 1° each layer. In the

LEGO Brick sample, we kept α constant for 50 layers before changing the scan angle. The angles we employed in the LEGO Brick sample were $0^\circ, 55^\circ,$ and 90° with respect to the X-axis, resulting in "bricks" with a $\{100\}, \{111\},$ and $\{011\}$ texture along the X direction, henceforth referred to as the $\{100\}\parallel X, \{111\}\parallel X,$ and $\{011\}\parallel X$ textured bricks, respectively. A schematic showing the scan strategy for the Helicoidal and LEGO Brick samples is shown in Fig. 1. We produced two Embedded Cylinder samples: a $\{111\}\parallel X$ textured cylinder of 0.6 mm diameter within a $\{100\}\parallel X$ textured cube and another one where the textures were swapped. To avoid disrupting the microstructure between areas of different textures, we manufactured all LEGO samples with a contourless printing strategy. All CAD files for the prints were prepared using MAGICS 21.0 (Materialise SA, Belgium).

After production, we cut samples from the base plate using wire

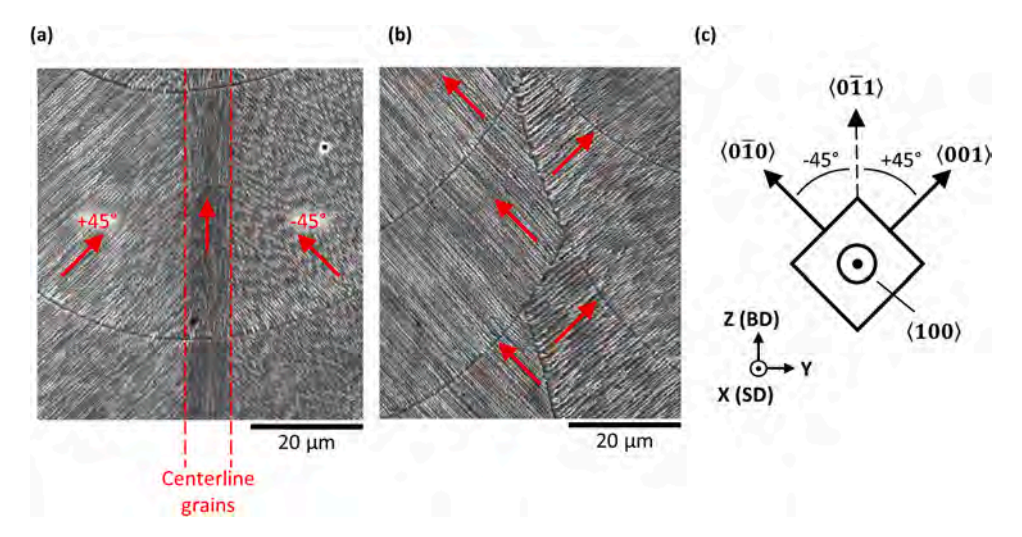


Fig. 2. (a) Secondary electron micrograph of stacked melt pools with the cells oriented with $\langle 100 \rangle$ along the BD in the centerline grains and \pm 45° to BD away from the centerline. (b) Secondary electron micrograph showing epitaxial growth between adjacent melt pools and layers. (c) Diagram of the typical grain orientation in the melt pool (excluding the centerline grains), which results from the bi-directional scan strategy.

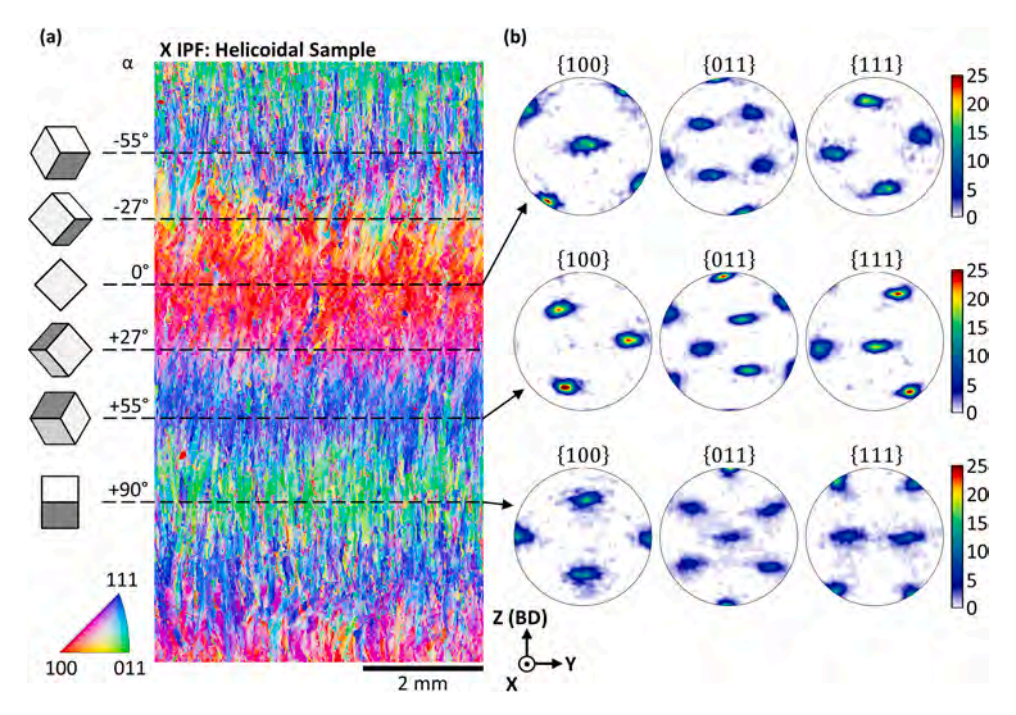


Fig. 3. Helicoidal sample (a) IPF map with respect to the X-axis and (b) selected pole figures for three layers with scan direction rotated $\alpha = 0^{\circ}$, 55° and 90° to the X-axis.

electrical discharge machining (Ichi Seiki, Singapore) and estimated their density using Archimedes test. All LEGO samples presented here have relative density of $99.5 \pm 0.1\%$ of the theoretical value for 316L.

We sectioned all samples along the Y-Z plane using a diamond saw and prepared the surface by grinding and polishing to 1 µm and then finishing with Struers Oxide Polishing Suspension (Struers OP-S) until a mirror-like surface was obtained. We then etched the samples for twenty minutes using Kroll's reagent. We characterized the microstructure on this cross-section by means of electron backscatter diffraction (EBSD). The helicoidal and LEGO-brick patterns were imaged using a Symmetry S2 detector (Oxford Instruments, UK) in a JEOL FESEM 7800F Prime with an accelerating voltage of 20 kV, probe current of 20 nA, and step size of 4 µm. The Embedded Cylinder samples were imaged using a Nordlys 2S detector (Oxford Instruments, UK) in a JEOL FESEM JSM 7600F with an accelerating voltage of 20 kV, probe current of 20 nA, and step size of 10 µm. We analyzed the data using the EBSD analysis software MTEX (Matlab 2020a) [9]. All pole figures were generated using de la Vallee Poussin kernels with a half-width of 2°. The small half-width was chosen as two times 1°, which corresponds to the texture rotation we expect to observe between subsequent layers in the Helicoidal sample.

3. Results

The nominal solidification structure of the LPBF 316L is shown in Fig. 2. This structure is commonly reported for AM 316L [10–12] and consists of colonies of elongated, solute-depleted columns—known as "cells"—bounded by solute-enriched dislocation walls that result from constitutional undercooling during rapid solidification. The cells grow preferentially along a $\langle 100 \rangle$ direction—the typical fast growth direction of cubic alloys [13]—which best matches the direction of the heat flow. By following the cell growth, we gain insight into how the solidification texture formed.

All the samples exhibit a strong $\left<0\overline{1}1\right>$ orientation with a minor periodic $\left<001\right>$ component along the BD. The resulting BD texture has been previously reported for AM 316L [8,14–16] as the result of heat flow within the melt pool and epitaxial growth between adjacent melt

pools. The key points are reiterated here. Within a given melt pool, thermal gradients develop across the solidification front. Along the melt pool centerline, the heat flow is vertical, and grains solidify with a $\langle 001 \rangle$ orientation along the BD (Fig. 2a). When the melt pool centerlines of subsequent layers align, these grains grow epitaxially along the BD. On either side of the centerline, the heat flows inward perpendicular to the curved melt pool walls and upward towards the melt pool surface. Here, grain growth does not necessarily occur along the maximum heat flow direction, but rather at \pm 45° to BD (Fig. 2a). This behavior has been previously observed in 316L [14,16,17] and other cubic alloys [18–20] and is attributed to side-branching of cells between overlapping melt pools. Much more energy is required for grain nucleation than grain growth, so it is energetically favorable for new cells to grow epitaxially along the $\langle 100 \rangle$ directions of existing cells. Cells growing at \pm 45° to BD are the optimum compromise for this epitaxial growth (Fig. 2b) and are thus preferentially selected. The resulting grains align two $\langle 100 \rangle$ axes along \pm 45° to BD and thus their $\langle 0\overline{1}1 \rangle$ orientation along BD.

Along the scan direction (SD), a $\{100\}$ \parallel SD texture with a minor periodic $\left\{1\overline{1}0\right\}$ \parallel SD component develops. The periodic component corresponds to the aforementioned centerlines and was also observed by Sun et al. [8]. As we demonstrate in the following sections, the $\{100\}$ \parallel SD texture is a result of epitaxial growth within the same layer due to the bi-directional scan strategy. Thus, the major component of the crystal-lographic texture is fixed with $\left\langle 0\overline{1}1\right\rangle$ along BD and $\left\langle 100\right\rangle$ along SD, as diagrammed in Fig. 2c. By keeping $\left\langle 0\overline{1}1\right\rangle$ orientation parallel to BD, the in-plane texture can be controlled simply by rotating the scan angle.

3.1. Helicoidal sample

Fig. 3a shows the inverse pole figure (IPF) map from the Y-Z cross-section of the Helicoidal sample. Grains are color-coded with respect to the X-axis (out of the cross-section plane). To observe the in-plane rotation, we divided the grain map into 40 μm (i.e. 1 layer) thick bins along the Z-axis and calculated a set of $\{100\}, \{011\},$ and $\{111\}$ pole figures across the full width of each bin. The sets at several selected

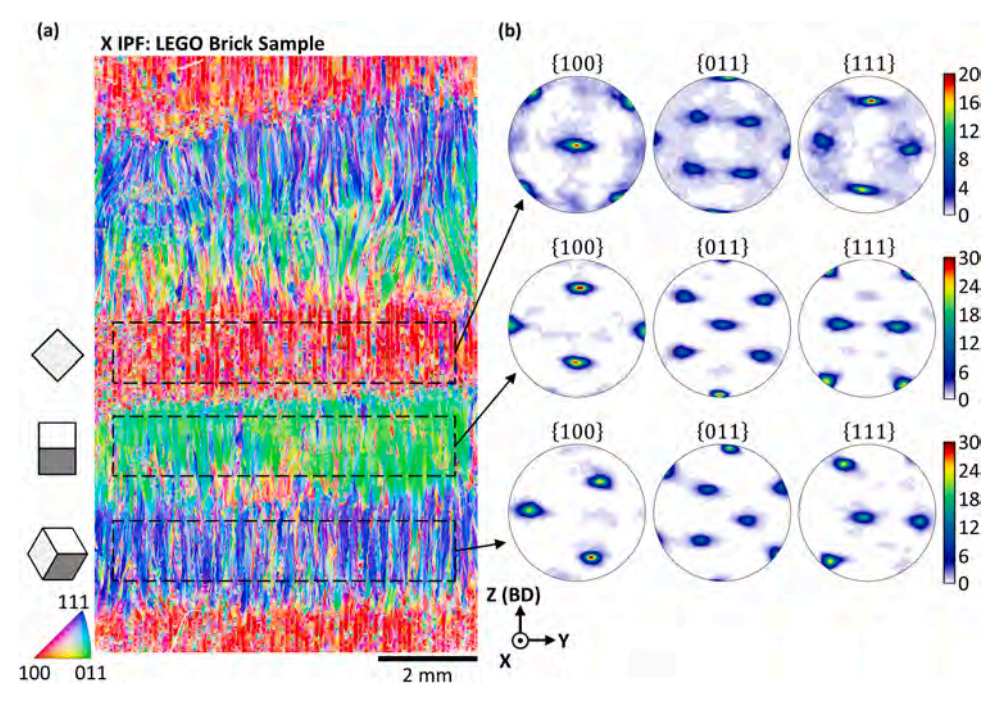


Fig. 4. LEGO Brick sample (a) IPF map with respect to the X-axis and (b) pole figures for a $\{100\} \parallel X$, $\{011\} \parallel X$, and $\{111\} \parallel X$ brick. The grains used to calculate the pole figures are bounded with dashed black lines.

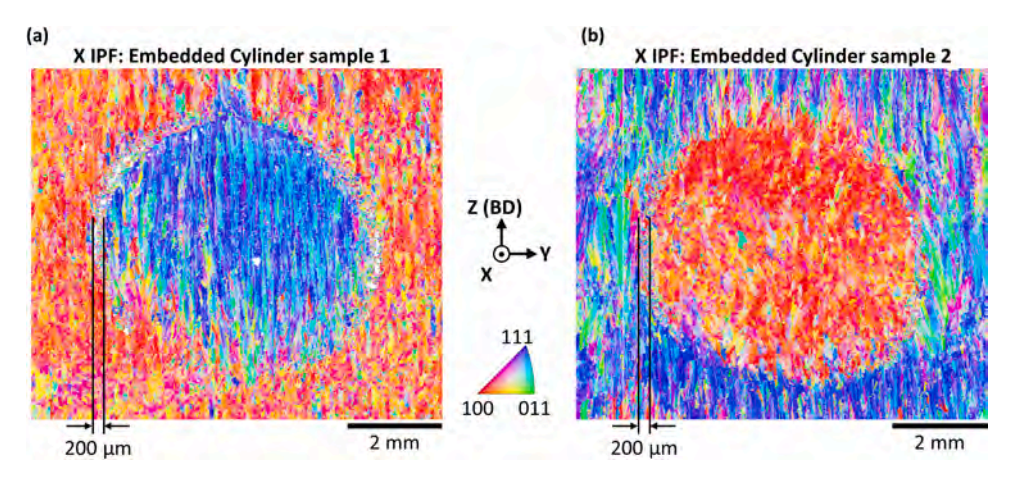


Fig. 5. IPF maps with respect to the X-axis for two Embedded Cylinder samples: (a) a $\{111\} \parallel X$ cylinder in a $\{100\} \parallel X$ cube and (b) a $\{100\} \parallel X$ cylinder in a $\{111\} \parallel X$ cube. The width of the transition region at the vertical interfaces is marked for both.

layers are shown in Fig. 3b, and an animated gif showing the progressive change in the pole figures along the Z-axis is included as a supplementary file online. The IPF map with respect to the Z-axis is included in the Appendix as Fig. A.1. As expected, all $\{011\}$ pole figures exhibit a strong peak at the poles of the Z-axis, indicating that the $\left<0\overline{1}1\right>$ orientation along the BD is maintained throughout the build. Other peaks appear that rotate about the Z-axis depending on the scan angle to the X-axis.

The pole figures show a $\{100\} \parallel X, \{111\} \parallel X,$ and $\{011\} \parallel X$ texture at scan angles of $0^{\circ}, 55^{\circ},$ and $90^{\circ},$ respectively, which confirm that a $\langle 100 \rangle$ texture develops along the SD (Fig. 3b). These angles are not random—rather, they correspond to the angles between the $\langle 100 \rangle$ direction and the $\langle 111 \rangle$ and $\langle 110 \rangle$ directions, which are 54.7° and 90°, respectively. This finding confirms that crystal orientation rotates about the $\left< 0\overline{1}1 \right>$ axis along the BD.

3.2. LEGO Brick and Embedded Cylinder samples

The IPF map with respect to the X-axis for the LEGO Brick sample is shown in Fig. 4a. The Z-axis IPF map is included in the Appendix as Fig. A.2. Each brick has a strong (> 20 times random) $\{100\} \parallel X, \{111\} \parallel X,$ or $\{011\} \parallel X$ texture. We produce these bricks by choosing a scan angle of $\alpha=0^{\circ},55^{\circ},$ and $90^{\circ},$ respectively, which we keep constant for 50 layers (2 mm). The corresponding crystal unit cells are diagrammed on the left of the IPF map. The respective pole figures for the three types of bricks are shown in Fig. 4b. Again, the $\{011\}$ pole figures show a strong peak along the Z-axis, confirming the $\left\langle 0\overline{1}1\right\rangle$ BD texture. Despite the strong texture, it is clear that "aberrant" grains—namely, grains which do not follow the desired "ideal" grain orientation—develop in each brick. Moreover, we note that the interfaces between different LEGO bricks are not sharp. It takes several layers to transition between bricks of different texture, with the transition length dependent on the textures in question. These two

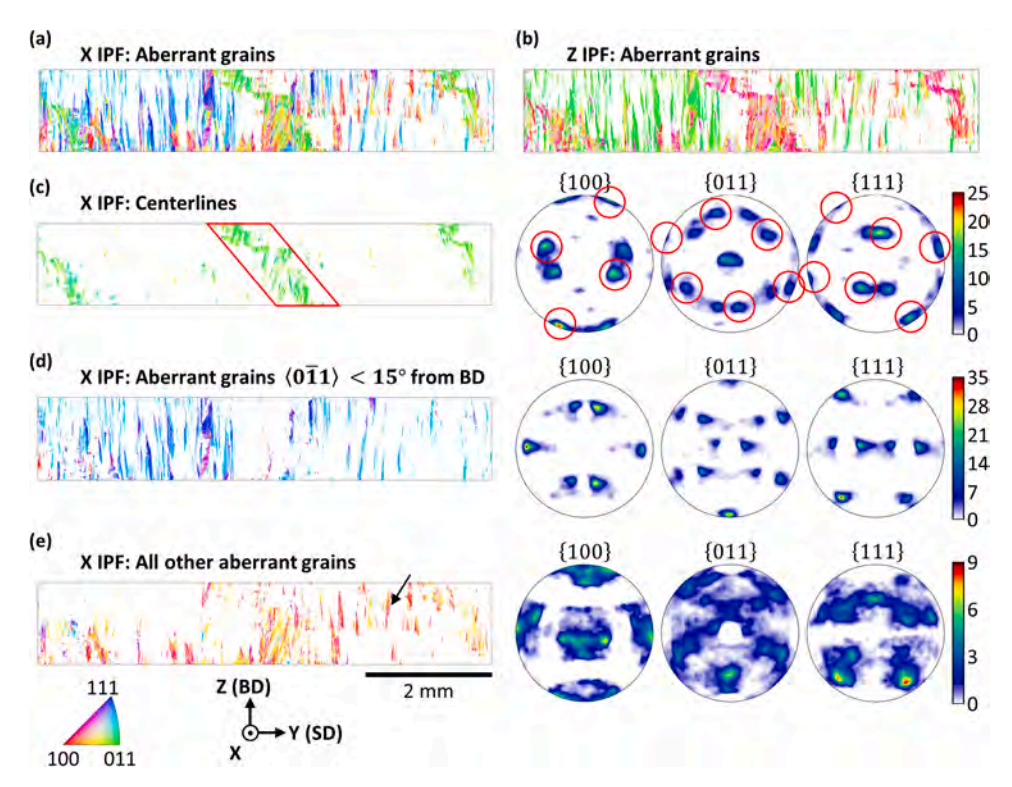


Fig. 6. Masked grain maps of the lower $\{011\} \parallel$ X LEGO brick. (a,b) IPF maps of aberrant grains with respect to the X- and Z-axes. (c,d,e) IPF maps with respect to the X-axis and accompanying pole figures for the centerline grains, aberrant grains with $\langle 0\overline{1}1\rangle < 15^\circ$ from BD, and the remaining aberrant grains. In (c), the peaks bounded in red in the pole figures correspond to the grains bounded in red in the IPF map. The arrow in the IPF map in (e) points to an aberrant grain which nucleates from a grain that was already growing in the desired orientation. (For interpretation of the references to colour in this figure legend, the reader is referred to the web version of this article.)

phenomena are discussed in detail in Sections 3.3 and 3.4.

IPF maps with respect to the X-axis for the two Embedded Cylinder samples are shown in Fig. 5. The Z-axis IPF map is included in the Appendix as Fig. A.3. Each sample has two distinct textured regions forming a cylinder inside of a cube. These samples demonstrate the ability to change the local texture point to point with a high spatial

resolution sufficient to produce curved interfaces. As with the LEGO Brick sample, we observe both aberrant grains and interface transition regions. The grain morphology at the interface changes from large, epitaxial grains at horizontal interfaces to fine, equiaxed grains at vertical interfaces. The transition at the vertical interfaces occurs over $\sim 200~\mu m$, corresponding to the width of two hatch spacings. This

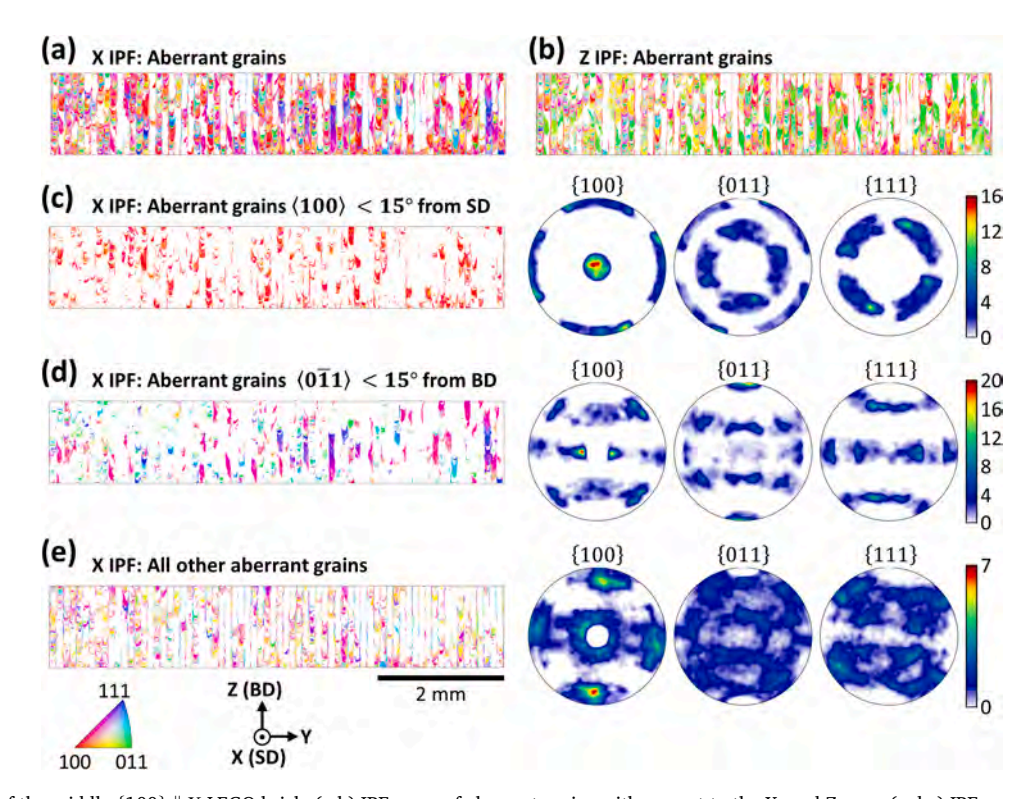


Fig. 7. Grain maps of the middle $\{100\} \parallel X$ LEGO brick. (a,b) IPF maps of aberrant grains with respect to the X- and Z-axes. (c,d,e) IPF maps with respect to the X- axis and accompanying pole figures for aberrant grains with $\langle 100 \rangle < 15^{\circ}$ from SD, aberrant grains with $\langle 0\overline{1}1 \rangle < 15^{\circ}$ from BD, and the remaining aberrant grains.

columnar-to-equiaxed transition (CET) occurs even though the laser parameters are kept the same—only the scan angle is changed across the interface. The origins of this CET and its implications are discussed in Section 4.

3.3. Aberrant grains

We define an aberrant grain as being misaligned from the desired grain orientation by > 15°, which is generally accepted as the misorientation angle across high angle grain boundaries. Due to the large misorientation, these grains may exhibit properties that differ significantly from the desired directional properties of the highly textured brick. Aberrant grains can be roughly divided into "systematic" and "stochastic" grains. The nucleation and growth of systematic aberrant grains can be explained by local thermodynamic variations that arise during expected processing conditions. Stochastic aberrant grains, on the other hand, arise from unpredictable variations in the processing conditions. In the following section, we applied masks to identify systematic and stochastic aberrant grains in the {100} || X and {011} || X LEGO bricks highlighted in Fig. 4. The aberrant grains in the $\{100\} \parallel X$ brick show their grain morphology and crystallography parallel to the scan direction. The aberrant grains in the $\{011\} \parallel X$ brick show their grain morphology and crystallography perpendicular to the scan direction.

The crystallography of the aberrant grains in the $\{011\} \parallel X$ LEGO brick is shown in Fig. 6. The LEGO Brick sample surface is not polished perfectly parallel to the Y-Z plane, but rather at a 2.47° counter-clockwise rotation about the axis $\langle 0, -0.685, 0.728 \rangle$. We calculated the tilt and rotation axis by measuring (x,y,z) coordinates for three corners of the sample in an SEM and then finding the angle between the resulting plane normal and the X-axis. Because of this tilt, three adjacent scan racks are bisected by the observation plane and thus are partially visible in Fig. 6. In this brick, the desired orientation is $\langle 011 \rangle \parallel X, \langle 100 \rangle \parallel Y$ (SD for this brick), and $\left\langle 0\overline{1}1 \right\rangle \parallel Z$ (BD). If we apply a mask that excludes all grains within 15° of this orientation, we are left with all of the aberrant grains (Fig. 6a and b). By this definition, 39% area fraction of the grains are considered aberrant.

If we further mask the aberrant grains to keep only those with $\langle 100 \rangle$ within 15° of the BD, we are left with the grains shown in Fig. 6c. Most of these grains are in three periodically spaced groups, the center of which is bounded by a red rhombus. With trigonometry we calculate that the groups are spaced ~ 101 µm apart along the X-axis, which corresponds almost exactly to our 100 µm hatch spacing. A diagram of the proof is included in the Appendix as Fig. A.4. Moreover, the grains are oriented with a $\langle 100 \rangle$ direction towards BD, which is consistent with the expected centerline grain growth direction in Fig. 2. Thus, we can conclude that these grains come from the centerlines of three adjacent melt tracks, which are visible because the tilted sample surface bisects the $\{011\} \parallel X$ LEGO brick at an angle. The pole figures show that these grains have two preferred orientations which arise from the bi-directional scan strategy. The middle centerline grains, marked by a red box, have a $\langle 100 \rangle$ direction + 10–15 $^{\circ}$ to the BD, as shown by the pole figures. The two other centerlines have a $\langle 100 \rangle$ direction - 10–15° to the BD. This result suggests that grains grow epitaxially at a ~ 10 – 15° angle to BD toward the scan direction, rather than directly parallel to BD as it has been reported in previous work [8]. The negative-positive-negative switching of the tilt direction results from the bi-directional line scans along -Y, +Y, and - Y, respectively. Since the nucleation and growth of the centerlines can be explained by predictable thermodynamic processes, we classify them as systematic aberrant grains.

If we mask the aberrant grains in Fig. 6a and b to keep only those with $\left<0\overline{1}1\right>$ within 15° of BD, we are left with the set of narrow, columnar grains that grow in between the centerlines, shown in Fig. 6d. The pole figures show that these grains all have a $\left<100\right>$ direction within

 $\pm~20^{\circ}$ of the Y-axis (SD). Grains may nucleate at an angle to the scanning direction due to the elliptical shape at the trailing edge of the melt pool [21]. Though they are misaligned with the SD, these grains are oriented with a fast-growth $\langle 100 \rangle$ direction $\sim~45^{\circ}$ to BD and therefore can easily grow epitaxially across layers, resulting in the columnar morphology.

The remaining aberrant grains in the $\{011\} \parallel X$ LEGO brick are shown in Fig. 6e and account for 12% of the total grains in the brick. As opposed to the previous two groups of grains, they do not seem to have a preferred orientation. We classify these as stochastic aberrant grains since there is no apparent reason why they would nucleate or grow. It should be noted that a large percentage of these grains appear to nucleate at the transition layer between two bricks, where the sharp change in heat flow direction may encourage nucleation of new grain orientations. However, this does not account for the aberrant grains which nucleate in the middle of the LEGO brick, for example the grain marked by an arrow in Fig. 6e. It is suspected that these grains may arise from stochastic local variations in melt pool thermodynamics, which we discuss in Section 4.

A similar masking process was applied to analyze the aberrant grains in a {100} || X brick. The {100} || X brick gives information about the grain morphology of a LEGO brick on a plane perpendicular to the {011} face. The IPF maps, masked maps, and corresponding pole figures for the middle {100} || X LEGO brick are shown in Fig. 7. The desired orientation is $\langle 100 \rangle \parallel X$ (SD for this brick), $\langle 011 \rangle \parallel Y$, and $\langle 0\overline{1}1 \rangle \parallel Z$. The aberrant grains are shown in Fig. 7a,b and comprise a 61% area fraction of the measured grains. If we apply a mask to keep only grains with $\langle 0\overline{1}1 \rangle$ within 15° of BD (Fig. 7d), we are left with a set of grains corresponding to the grains we observed in Fig. 6d. As expected, these grains are preferentially oriented with a (100) direction within \pm 15–20° of the SD. There are also tall, narrow grains corresponding to the centerlines visible in Fig. 7c and e. Apart from the grains in Fig. 7d, there are no apparent trends in the rest of the aberrant grains. These will be classified as stochastic aberrant grains. It is worth noting that no grains, aberrant or otherwise, grow laterally in the same layer for more than one hatch spacing. Thus, the centerlines appear to act as natural barriers to epitaxial growth within the layer.

To elucidate how stochastic aberrant grains form, we examined the crystallographic orientation and accompanying cell structures of several such grains from the {100} || X LEGO brick (Fig. 8). The cells show that new grains nucleate from the sides of the melt pools and grow towards the centerlines. These new grains are often re-melted by subsequent scans and can grow epitaxially if they have a $\langle 100 \rangle$ axis near the local thermal gradient, as the energy barrier for nucleation is lower than that for nucleation [18]. This phenomenon may result in the formation of grains with relatively large misorientation (> 15°) with respect to the desired orientation. This phenomenon is observed, for example, at the intersection of melt pools marked "A" in Fig. 8b. The new grain nucleates high up the wall of melt pool 3 and grows perpendicular to the wall, which is consistent with LPBF literature showing that grains grow perpendicular to the solidification front, inward and towards the incident laser beam [8,22,23]. Side-branching at 90° to the original growth direction allows the grain to continue growing epitaxially for several layers (from melt pools 3 through 12), resulting in a chevron shape. Similar nucleation events are visible at points marked "B", "C", and "D" in Fig. 8b.

New orientations may also nucleate along the solidification front when the inherited grain orientation is poorly oriented for the new heat flow, as at point E in melt pool 22 (Fig. 8b). Grains grow epitaxially from melt pools 20 and 21 until a new, better-aligned grain nucleates and dominates the solidification. The occurrence of grain nucleation away from the melt pool boundary suggests that grain growth in melt pools 20 and 21 was slow enough to allow nucleation ahead of the solidification front. However, nucleation from the melt pool walls is more commonly observed in the $\{100\} \parallel X$ LEGO brick.

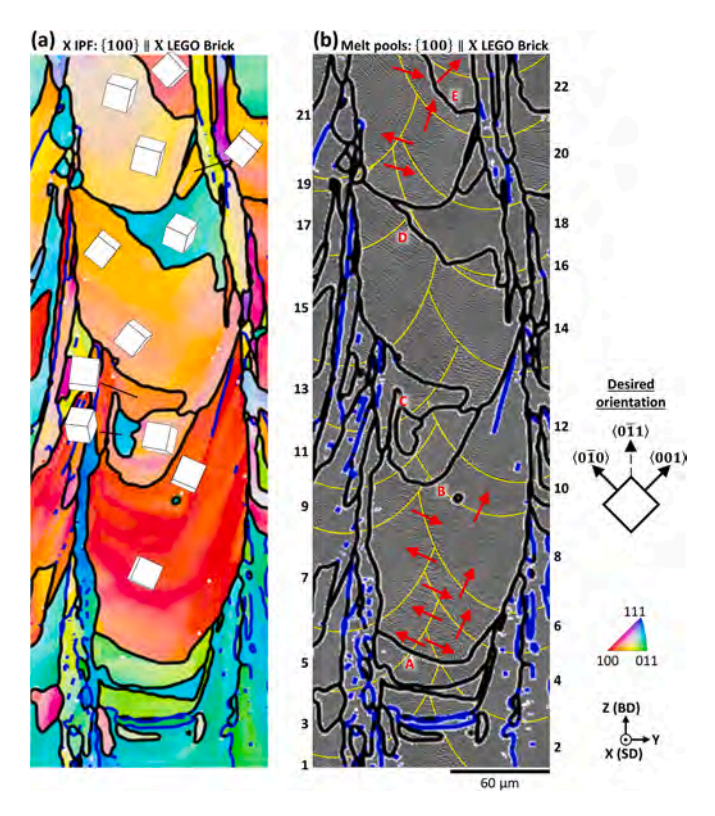


Fig. 8. Aberrant grains in the $\{100\} \parallel X$ LEGO brick. (a) IPF map with respect to the X-axis and (b) secondary electron micrograph of the same grains. Grain boundaries with misorientation between $7^{\circ}-15^{\circ}$ are marked in blue and $>15^{\circ}$ in black. The unit cell orientation is shown for each aberrant grain in the IPF maps. In the secondary electron micrograph, melt pool boundaries are highlighted in yellow and numbered in the order they are formed. The grain growth direction in the Y-Z plane is marked for some grains by red arrows. (For interpretation of the references to colour in this figure legend, the reader is referred to the web version of this article.)

Fig. 8 suggests that the melt pool morphology strongly influences the prevalence of stochastic aberrant grains. The melt pools in Fig. 8b are far from the uniformly spaced and vertically aligned melt pools we observed in Fig. 2. They are slightly misaligned across subsequent layers and penetrate to different depths even within the same layer. For example, melt pools 15 and 16 belong to the same layer, but melt pool 16 penetrates $\sim55\,\mu m$ less than 15. Consequently, it does not overlap melt pool 15 as much, allowing an aberrant grain near the top of melt pool 15 to survive at the point marked "D" (Fig. 8b). The grain then grows epitaxially into melt pools 16–18. The irregular melt pool geometry also suggests that the local heat flow conditions can vary significantly across different melt pools, which may explain why highly misoriented grains are able to grow epitaxially through several melt pools.

3.4. Diffuse Interfaces

In the LEGO Brick and Embedded Cylinder samples, the transition between regions of distinct texture occurs over several layers, resulting in a "diffuse" interface. We observe this phenomenon, for example, at the $\{011\} \rightarrow \{100\} \parallel X$ interface, where α changes by 90° . An IPF map of this interface is shown in Fig. 9a. Despite the 90° rotation of the thermal gradient, most of the grains in the first five to six layers epitaxially grow from the underlying $\{011\} \parallel X$ LEGO brick. The only obvious grain

nucleation occurs at melt pool centerlines, which divide the $\{100\} \parallel X$ LEGO brick into columns comprising two overlapping half-scan tracks. New grains nucleate by the same mechanisms described in Section 3.3 until a grain that is favorably oriented to the new thermal gradient dominates the growth. This selection process can occur quickly, as in columns "A" and "B", or require many layers, as in columns "C" and "D" (Fig. 9).

To quantify the number of layers it takes to switch to the new desired grain orientation we calculate the misorientation angle, which defines the shortest single rotation in three-dimensional space, between each 4 μ m \times 4 μ m pixel and the ideal {100} \parallel X, {011} \parallel X, and {111} \parallel X orientations. We then average the values for each layer (10 rows of pixels) and plot these angles as a function of the layer distance from the scan angle change. The results for the $\{011\}\rightarrow\{100\} \parallel X$, $\{100\} \rightarrow \{111\} \parallel X$, and $\{111\} \rightarrow \{011\} \parallel X$ interfaces are shown in Fig. 9b,c, and d, respectively. To account for curved interfaces (noticeable in Fig. 4a), we divide the EBSD dataset into 20 bins of equal width along the Y-axis. The pixel at which the scan angle changes is determined separately for each bin by analyzing the melt pool shape in the Y-Z plane using optical microscopy. We consider the texture transition complete when the orientation stops changing (illustrated in Fig. 9b,c, d by the vertical, dashed lines). To identify this point consistently across all interfaces, we calculate the moving average of the first derivative of the misorientation angles and consider the texture transition complete when the rate of change of all three misorientation angles is below 0.25° per layer. The moving average was calculated with periods from 5 to 11 and the mean number of transition layers was determined to be 19 ± 2.2 , to 23 ± 0.52 , to 28 ± 2.0 layers (95% confidence interval) for $\Delta \alpha = 35^{\circ}$, 55° , and 90° , respectively.

Although the number of layers required for texture transition appears to increase with $\Delta \alpha$, there is a "lag" of several layers before the average texture changes noticeably at some of the interfaces. At the $\{011\} \rightarrow \{100\} \parallel X$ interface, for instance, the texture stays consistent for \sim 6 layers after changing α , implying that epitaxial growth continues despite the large $\Delta \alpha = 90^{\circ}$. This phenomenon can also be visually observed in Fig. 9a. Similarly, the texture at the $\{100\}\rightarrow\{111\}\parallel X$ interface is maintained for ~ 2 layers before showing appreciable changes. Conversely, the average texture begins to change immediately after α is changed across the $\{111\} \rightarrow \{011\} \parallel X$ interface. Not considering this "lag", the number of transition layers becomes comparable across all three interfaces, between 19 and 21 layers. These results suggest that texture must change more quickly as $\Delta \alpha$ increases to accommodate the larger misorientation over the same distance. Indeed, the interfaces with a higher $\Delta \alpha$ appear qualitatively sharper in the LEGO Brick sample (Fig. 4). The sharpness of the transition can be correlated to the grain morphology across the interfaces. At the $\{011\} \rightarrow \{100\} \parallel X$ interface, new grain orientations nucleate layer by layer as shown in Fig. 9a. At the $\{111\} \rightarrow \{011\} \parallel X$ interface, however, many large grains are observed to grow epitaxially across the interface, slowly twisting about BD until they match the new desired orientation. A mixture of both types of grains is observed at the $\{111\} \rightarrow \{100\} \parallel X$ interface. The slowly rotating grains result in a more gradual qualitative transition between textures.

4. Discussion

In this paper, we present a scan strategy for site-specific texture control in LPBF 316L. The crystallographic texture of a polycrystalline metal governs a wide range of materials properties, including strength, ductility, toughness, corrosion resistance, and electromagnetic susceptibility [24]. By controlling texture point to point via LPBF, we can

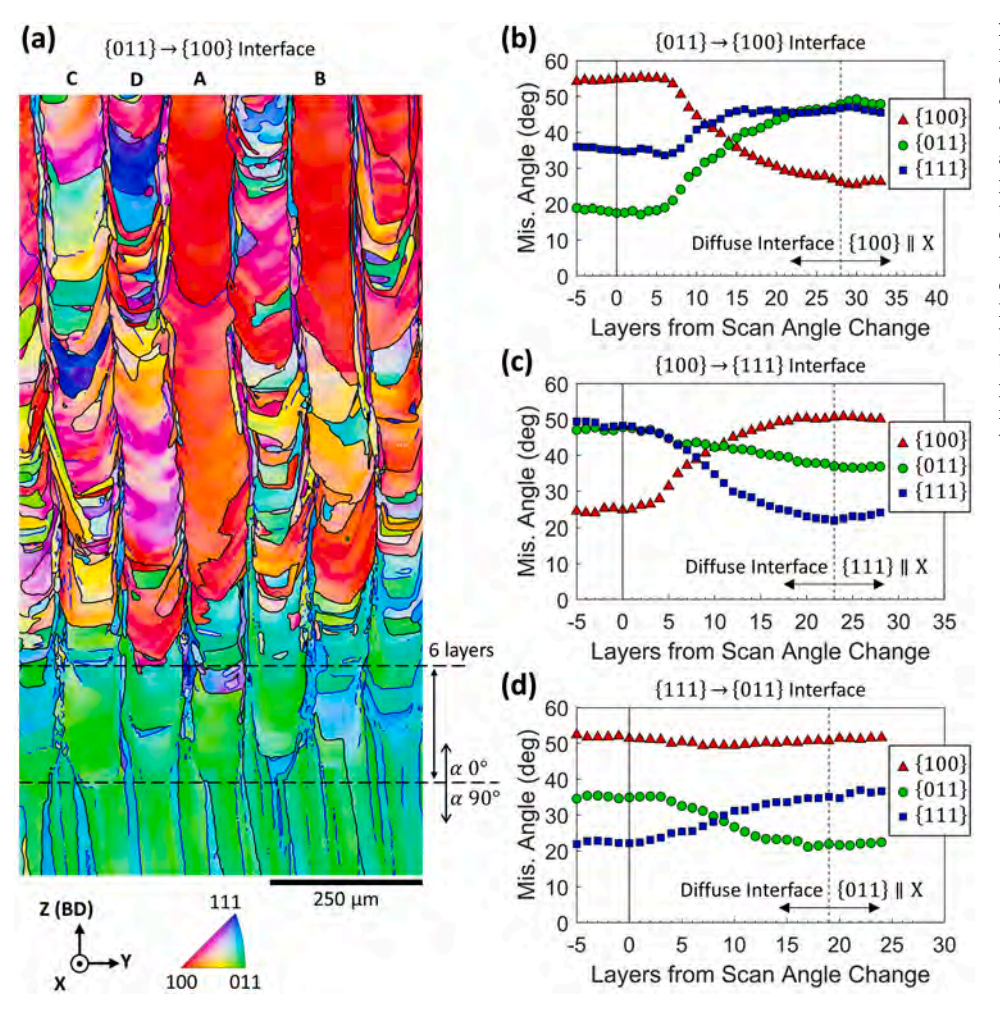


Fig. 9. Interfaces in the LEGO-brick sample. (a) IPF map of the $\{011\}\rightarrow\{100\} \parallel X$ interface. Grain boundaries with misorientation between $7^{\circ}-15^{\circ}$ are marked in blue and $>15^{\circ}$ in black. "A" and "B" mark two columns bounded by adjacent centerlines that transition to the preferred {100} || X brick orientation within the imaged area. (b,c,d) Average of the misorientation angles between the EBSD pixels and the ideal $\{100\} \parallel X$, $\{011\} \parallel X$, and $\{111\} \parallel X$ orientations as a function of the number of layers from where the scan angle changed (from bottom up). Negative numbers indicate layers before the scan angle is changed. (For interpretation of the references to colour in this figure legend, the reader is referred to the web version of this article.)

construct functionally graded components with spatially varying properties [2]. Using our scan strategy, we build bricks of different shape and strong texture by a repeated, bi-directional scan pattern that does not

translate or rotate between layers. Each brick has a strong $\left\{0\overline{1}1\right\}\parallel BD$ texture. We demonstrate that the texture perpendicular to the BD can be controlled by simply rotating the laser scan angle and showcase this

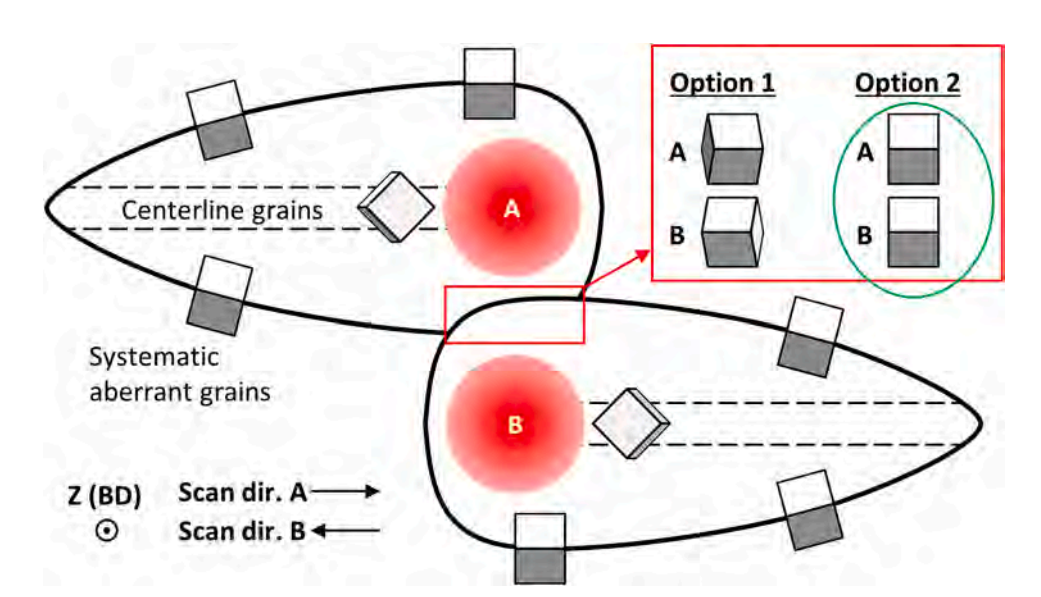


Fig. 10. Schematic of the selection mechanism during bi-directional scanning that results in a $\langle 100 \rangle$ texture along the scan direction. Examples of how systematic aberrant grain orientations could nucleate from the elongated melt pool tail are also shown.

capability by printing a rotating crystal (Fig. 3, Appendix GIF A.1), strongly textured rectilinear layers (Fig. 4), and cylinders with curved interfaces (Fig. 5).

Our LEGO strategy greatly expands the scope of AM as a tool for building functionally graded materials. AM research into functionally graded materials has largely focused on varying alloy composition [4, 25,26] or grain size and morphology [27] to build components with gradient materials properties. Our LEGO strategy makes it possible to generate gradient material properties in a single alloy or to augment the materials properties in combination with graded alloy composition. Functionally graded materials with large regions of distinct properties have been explored less but represent a field with vast potential. Popovich et al. [28] printed single components of Inconel 718 with regions of fine, equiaxed grains and coarse, elongated grains which showed sharp transitions in mechanical properties. Coarse- and fine-grained bimodal microstructures have also been used to encode information in AM microstructures, including text [6,16], artwork [29], and recently a QR data matrix [30]. These studies were limited to two distinct microstructures, whereas the LEGO strategy can produce dozens of distinct microstructures limited only by the measurement technique.

The LEGO strategy relies on intra-layer epitaxial growth due to the bi-directional scan strategy that creates a {100} texture along SD. The {100} || SD texture has been previously reported in 316L [8,15,16] and other cubic alloys [5,19,20,31]. Geiger et al. [5] used an alternating 90° rotation strategy during LPBF of Inconel 738 to induce a strong cube texture with the $\langle 100 \rangle$ axis parallel to the BD. They built samples with regions of $\langle 100 \rangle$ and $\langle 110 \rangle$ texture perpendicular to the BD by scanning parallel/perpendicular to the reference direction or $-45^{\circ}/+45^{\circ}$ to the reference direction, respectively. Other studies using the bi-directional scan strategy [15,31] attribute the {100} || SD texture to backwards flow of liquid melt driven by hydrodynamic forces. However, these explanations fail to explain why uni-directional scan strategies do not also result in a {100} texture along the SD for cubic alloys [18,32,33]. Analysis of the LEGO Brick sample (Section 3.2) shows that the centerlines of the melt pools grow at 10-15° to the BD towards the SD, suggesting that the maximum heat flow is also inclined towards the SD. Under a uni-directional scan strategy, the melt between the centerlines would also be expected to solidify with the $\left\langle 0\overline{1}1\right\rangle$ direction oriented at this tilt, as has been observed in DED [18]. A simpler explanation is that the 180° rotation of the "serpentine" scan strategy preferentially selects grains with a $\langle 100 \rangle$ direction along SD as the only way to conserve the crystal orientation for epitaxial growth between two adjacent scan lines. The growth mechanism is diagrammed in Fig. 10, in which the SD, and thus the heat flow, reverses with each subsequent pass. Grains with $\left< 0\overline{1}1 \right> \|$ BD can grow epitaxially during both the forward and backward scans according to the \pm 45° mechanism reported in literature [8,14,17] and are thus preferentially selected during solidification. Thus, we expect this mechanism be the dominant reason for the {100} || SD texture, as opposed to the effect of hydrodynamic forces. The method of promoting epitaxial growth within a layer and between subsequent layers should be applicable to a wide range of AM metals.

Although each LEGO brick exhibits strong texture, we observe grains that are misaligned from the desired orientation. These aberrant grains are consistently observed when trying to prepare single crystals by AM, both for 316L [8,17,34,35] and other metals [5,19,20,28]. However, their origins are rarely addressed. Here, we identify two types of aberrant grains: systematic and stochastic. Systematic aberrant grain formation can be reduced by changing the processing parameters. Sun et al. [8] showed that the centerline grains can be eliminated by increasing

the energy density to switch from conduction to keyhole mode. A second set of systematic aberrant grains was identified in the LEGO Brick sample and attributed to the angled heat flow at the back of the melt track (Fig. 10). Elongating the melt pool—for example by scanning at higher speeds or reducing the spot size—could reduce the average misorientation angle to the desired orientation.

We observe stochastic aberrant grains that nucleate along the sides of the melt pools. Studies of melt pool solidification for 316L [22] and other metals [23] show that multiple grains can nucleate and grow perpendicular to the solidification front. In multi-layer prints, grains near the bottom of the melt pool often inherit their orientation through epitaxial growth and subsequent layers will re-melt stray grains formed near the surface of the melt pool. If they are not fully re-melted, these stray grains may grow epitaxially into subsequent melt pools to form aberrant grains (Fig. 8). Misaligned and irregular melt pools will also increase the likelihood that stray grains are not re-melted. These results suggest that increasing re-melting, for example by decreasing layer thickness or hatch spacing, should reduce the amount of aberrant grains.

Annealing during or after the print may also help reduce aberrant grains. Körner et al. [36] produced highly homogeneous, defect-free single crystals of Ni-based superalloy CMSX-4 by EBM. The print chamber was kept at 1000 °C during the print, resulting in an in-situ annealing effect. However, heat treatments may cause undesirable recrystallization at interfaces between textured bricks. For example, Geiger et al. [5] observed a significant weakening of texture after heat-treating strongly-textured blocks of Inconel 738 produced by SLM. The effect of heat treatment on such strongly textured LEGO bricks warrants further research.

Our work also examines the interfaces between distinct textured regions for the first time. A significant finding is that the morphology and transition length of the interface varies with its orientation, as shown by the Embedded Cylinder samples (Fig. 5). The horizontal interfaces have a columnar morphology with grains growing epitaxially across the interface for several layers. The vertical interfaces are no more than two scan tracks wide and have a fine, equiaxed morphology. The different morphologies suggest that the thermal gradient is much stronger along the BD than the SD. Thus, there is a significantly stronger driving force for epitaxial growth across horizontal interfaces than across vertical interfaces. The observed CET between the horizontal and vertical interfaces also implies that CET can be achieved simply by changing the scan angle. Typically, CET is achieved by manipulating the laser energy density to change the magnitude of the thermal gradient G and solidification rate R [6,7,28,37]. In the Embedded Cylinder samples, however, the process parameters are constant across the interface. Thus, the change in scan angle must be responsible for the local change in solidification conditions. Without the bi-directional overlap of adjacent scan lines described in Fig. 10, the driving force for epitaxial growth within a layer is lost. In Fig. 5, this results in the repeated nucleation of grains with no preferred orientation, implying that we can transition between columnar and equiaxed grains without changing the energy density by switching scanning direction multiple times within a layer. This method should be applicable to any material and fusion-based AM technique. It should also be noted that lack-of-fusion porosity is observed in the Embedded Cylinder sample in Fig. 5a, although not in the sample in Fig. 5b. Porosity can affect the local heat flow since the thermal conductivity of loose powder with entrapped gas is orders of magnitude lower than solid 316L [38]. Further research is warranted to determine the potential influence of porosity on the observed CET.

We also observed that a larger change in scan angle results in a qualitatively sharper transition between regions of distinct textures that is correlated to the grain selection mechanism at the interface. At the $\{011\} \leftrightarrow \{100\} \parallel X$ interfaces, the new texture is achieved entirely by the stochastic nucleation and selection process of new grain orientations, as described in Section 3.3. At the other interfaces, however, we observe some grains that continue to grow epitaxially while rotating to the new desired orientation. Similar twisting, columnar grains were observed in DED-prepared 304L steel, with internal misorientation changes of up to 1° every $21\text{--}24\,\mu\text{m}$ [39]. This additional mechanism can explain why the texture transition occurs more gradually as $\Delta\alpha$ is decreased. It is worth noting that, even under the maximum $\Delta\alpha=90^\circ$, epitaxial growth occurs over five to six layers before widespread nucleation of new grain orientations occurs. This finding reinforces the idea that the thermal gradient is much stronger along the BD than along the other two directions.

5. Conclusions

In this paper we present a bi-directional scan strategy for controlling texture perpendicular to the build direction for LPBF stainless steel 316L. The main findings are summarized below:

- 1. Our LEGO strategy can build components with a gradient texture and components with distinct regions of strong texture (15–35 times random) separated by linear and curved interfaces.
- 2. The strong texture arises from inter-layer epitaxial growth at \pm 45° to BD and epitaxial growth within each layer due to the bi-directional scan strategy that aligns $\left\langle 0\overline{1}1\right\rangle$ along BD and $\left\langle 100\right\rangle$ along SD, respectively.
- 3. Despite the strong texture, we observe "aberrant" grain orientations with undesirable crystallographic orientations. These grains nucleate near the upper part of melt pools and are not fully re-melted by subsequent layers, allowing them to grow epitaxially.
- 4. The morphology and transition length of the interface between two regions with different scan angles depends on the change in orientation. Columnar grains grow epitaxially across horizontal interfaces due to the strong thermal gradient along BD. We observe a region of fine, equiaxed grains which is no more than one scan track wide at vertical interfaces. We attribute the origin of these regions to the abrupt rotation of the thermal gradient about BD, which misaligns the re-melted grains for epitaxial growth and thus favors nucleation of new grain orientations.
- 5. The columnar-to-equiaxed transition (CET) observed between the interfaces implies that CET can be achieved by simply switching the scan angle repeatedly within one layer, without changing the imparted energy density.

The techniques presented here can be extended to other alloy systems and should significantly expand the scope of AM for creating functionally graded materials.

CRediT authorship contribution statement

Karl A. Sofinowski: Validation, Investigation, Formal analysis, Writing - original draft, Visualization. Sudharshan Raman: Conceptualization, Methodology, Writing - review & editing. Xiaogang Wang: Validation, Investigation, Formal analysis, Writing - review & editing. Bernard Gaskey: Conceptualization, Methodology. Matteo Seita: Conceptualization, Supervision, Project administration, Funding acquisition, Writing - review & editing.

Declaration of Competing Interest

The authors declare the following financial interests/personal relationships which may be considered as potential competing interests: This work was funded by the National Research Foundation (NRF)

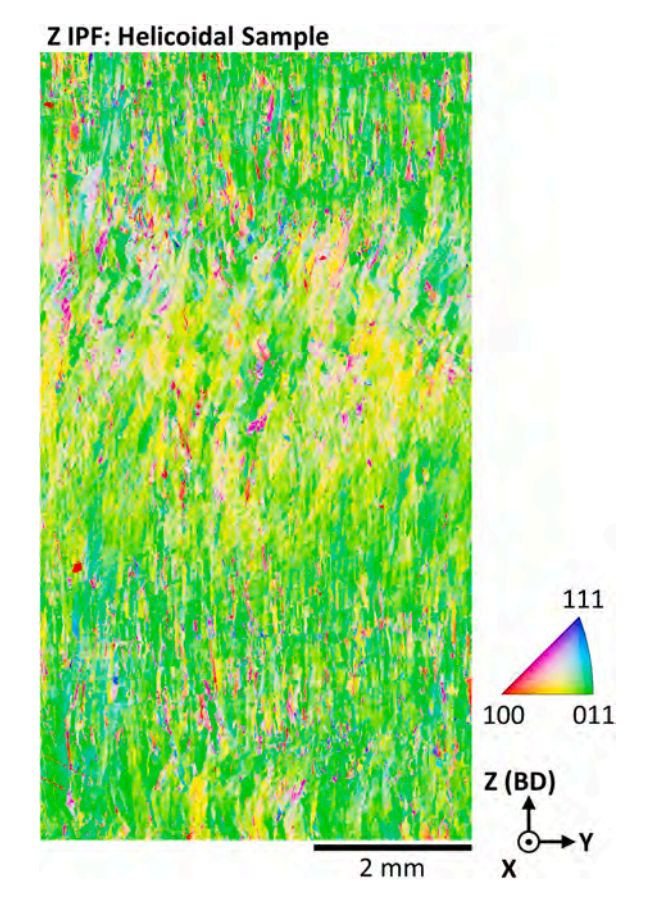


Fig. A.1. Helicoidal sample IPF map with respect to the Z-axis.

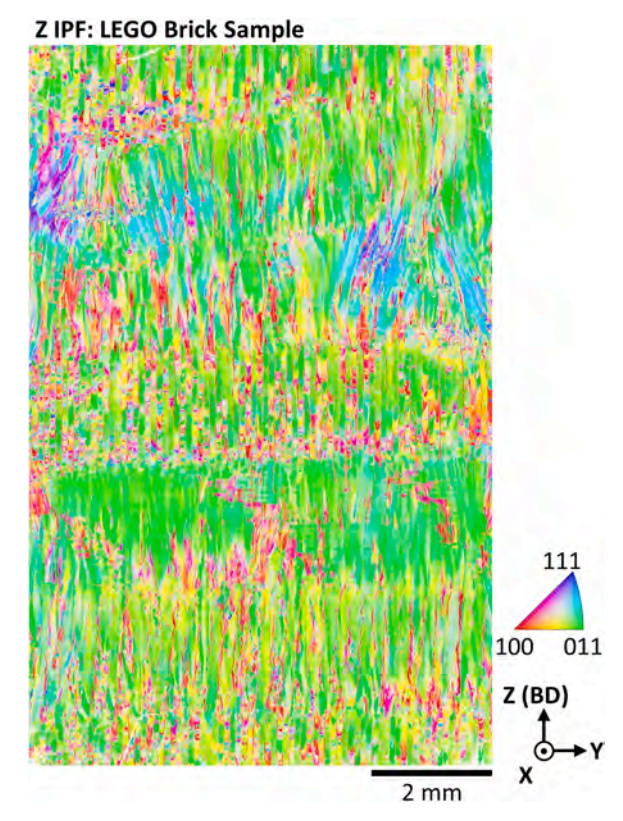


Fig. A.2. LEGO Brick sample IPF map with respect to the Z-axis.

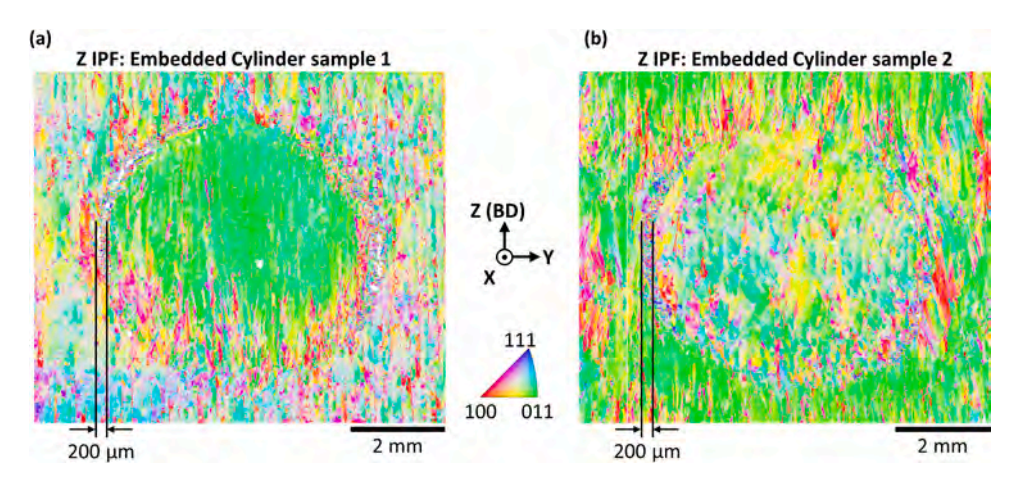


Fig A.3. IPF maps with respect to the Z-axis for two Embedded Cylinder samples: (a) a $\{111\} \parallel X$ cylinder in a $\{100\} \parallel X$ cube and (b) a $\{100\} \parallel X$ cylinder in a $\{111\} \parallel X$ cube.

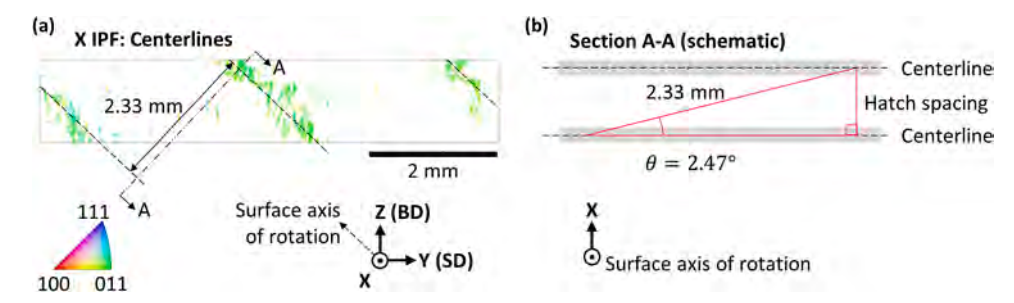


Fig A.4. Diagrams showing the method for identifying the aberrant grains in Fig. 6c as centerline grains. (a) Aberrant grains from Fig. 6c with the axis of rotation of the surface overlaid. (b) Schematic of Section A-A from Fig. A.4a, showing the trigonometric relationship between the hatch spacing and surface plane.

Singapore, under the NRF Fellowship programme (NRF-NRFF2018-05) and the NTU-CSIRO seed fund.

Acknowledgements

The authors would like to acknowledge Sri Lathabai and Darren Fraser of the Commonwealth Scientific and Industrial Research Organisation (CSIRO) in Australia for their inputs and stimulating discussions, as well as Ekta Jain and Shubo Gao from the AddME lab at NTU for their help with sample characterization. This work was supported by the National Research Foundation (NRF) Singapore, under the NRF Fellowship program (NRF-NRFF2018–05) and the NTU-CSIRO seed fund. Access to shared experimental facilities used in this work was provided by the School of Mechanical and Aerospace Engineering and the Facility for Analysis Characterisation Testing and Simulation at NTU.

Appendix A

Appendix.

Appendix B. Supporting information

Supplementary data associated with this article can be found in the online version at doi:10.1016/j.addma.2020.101809.

References

- [1] W.E. Frazier, Metal additive manufacturing: a review, J. Mater. Eng. Perform. 23 (2014) 1917–1928, https://doi.org/10.1007/s11665-014-0958-z.
- [2] V.A. Popovich, E.V. Borisov, A.A. Popovich, V.S. Sufiiarov, D.V. Masaylo, L. Alzina, Functionally graded Inconel 718 processed by additive manufacturing:

- crystallographic texture, anisotropy of microstructure and mechanical properties, Mater. Des. 114 (2017) 441–449, https://doi.org/10.1016/j.matdes.2016.10.075.
- [3] C.J. Todaro, M.A. Easton, D. Qiu, D. Zhang, M.J. Bermingham, E.W. Lui, M. Brandt, D.H. StJohn, M. Qian, Grain structure control during metal 3D printing by highintensity ultrasound, Nat. Commun. 11 (2020) 1–9, https://doi.org/10.1038/ s41467-019-13874-z.
- [4] S. Tammas-Williams, I. Todd, Design for additive manufacturing with site-specific properties in metals and alloys, Scr. Mater. 135 (2017) 105–110, https://doi.org/ 10.1016/j.scriptamat.2016.10.030.
- [5] F. Geiger, K. Kunze, T. Etter, Tailoring the texture of IN738LC processed by selective laser melting (SLM) by specific scanning strategies, Mater. Sci. Eng. A 661 (2016) 240–246, https://doi.org/10.1016/j.msea.2016.03.036.
- [6] R.R. Dehoff, M. Kirka, W.J. Sames, H. Bilheux, A.S. Tremsin, L.E. Lowe, S.S. Babu, Site specific control of crystallographic grain orientation through electron beam additive manufacturing, Mater. Sci. Technol. (U. Kingd.) 31 (2015) 931–938, https://doi.org/10.1179/1743284714Y.0000000734.
- [7] H. Helmer, A. Bauereiß, R.F. Singer, C. Körner, Grain structure evolution in Inconel 718 during selective electron beam melting, Mater. Sci. Eng. A 668 (2016) 180–187, https://doi.org/10.1016/j.msea.2016.05.046.
- [8] S.H. Sun, T. Ishimoto, K. Hagihara, Y. Tsutsumi, T. Hanawa, T. Nakano, Excellent mechanical and corrosion properties of austenitic stainless steel with a unique crystallographic lamellar microstructure via selective laser melting, Scr. Mater. 159 (2019) 89–93, https://doi.org/10.1016/j.scriptamat.2018.09.017.
- [9] F. Bachmann, R. Hielscher, H. Schaeben, Texture analysis with MTEX free and open source software toolbox, Solid State Phenom. 160 (2010) 63–68, https://doi. org/10.4028/www.scientific.net/SSP.160.63.
- [10] Y.M. Wang, T. Voisin, J.T. McKeown, J. Ye, N.P. Calta, Z. Li, Z. Zeng, Y. Zhang, W. Chen, T.T. Roehling, R.T. Ott, M.K. Santala, P.J. Depond, M.J. Matthews, A. V. Hamza, T. Zhu, Additively manufactured hierarchical stainless steels with high strength and ductility, Nat. Mater. 17 (2018) 63–71, https://doi.org/10.1038/nmat5021
- [11] Y. Zhong, Sub-Grain Structure in Additive Manufactured Stainless Steel 316L, Stockholm University, 2017. Accessed May 8 2020, http://urn.kb.se/resolve? urn=urn.php/se/su/diva-144519
- [12] L. Liu, Q. Ding, Y. Zhong, J. Zou, J. Wu, Y.-L. Chiu, J. Li, Z. Zhang, Q. Yu, Z. Shen, Dislocation network in additive manufactured steel breaks strength-ductility tradeoff, Mater. Today 21 (2018) 354–361, https://doi.org/10.1016/j. matted 2017.11.004
- [13] W.A. Tiller, Preferred growth direction of metals, JOM 9 (1957) 847–855, https://doi.org/10.1007/BF03397928.

- [14] M.S. Pham, B. Dovgyy, P.A. Hooper, C.M. Gourlay, A. Piglione, The role of side-branching in microstructure development in laser powder-bed fusion, Nat. Commun. 11 (2020) 1–12, https://doi.org/10.1038/s41467-020-14453-3.
- [15] O. Andreau, I. Koutiri, P. Peyre, J.D. Penot, N. Saintier, E. Pessard, T. De Terris, C. Dupuy, T. Baudin, Texture control of 316L parts by modulation of the melt pool morphology in selective laser melting, J. Mater. Process. Technol. 264 (2019) 21–31, https://doi.org/10.1016/j.jmatprotec.2018.08.049.
- [16] J.J. Marattukalam, D. Karlsson, V. Pacheco, P. Beran, U. Wiklund, U. Jansson, B. Hjörvarsson, M. Sahlberg, The effect of laser scanning strategies on texture, mechanical properties, and site-specific grain orientation in selective laser melted 316L SS, Mater. Des. 193 (2020), 108852, https://doi.org/10.1016/j.matdes.2020.108852
- [17] O. Andreau, I. Koutiri, P. Peyre, J.-D. Penot, N. Saintier, E. Pessard, T. De Terris, C. Dupuy, T. Baudin, Texture control of 316L parts by modulation of the melt pool morphology in selective laser melting, J. Mater. Process. Technol. 264 (2019) 21–31, https://doi.org/10.1016/j.jmatprotec.2018.08.049.
- [18] H.L. Wei, J. Mazumder, T. DebRoy, Evolution of solidification texture during additive manufacturing, Sci. Rep. 5 (2015) 1–7, https://doi.org/10.1038/ srep16446
- [19] S.H. Sun, K. Hagihara, T. Nakano, Effect of scanning strategy on texture formation in Ni-25 at%Mo alloys fabricated by selective laser melting, Mater. Des. 140 (2018) 307–316, https://doi.org/10.1016/j.matdes.2017.11.060.
- [20] T. Ishimoto, K. Hagihara, K. Hisamoto, S.-H. Sun, T. Nakano, Crystallographic texture control of beta-type Ti-15Mo-5Zr-3Al alloy by selective laser melting for the development of novel implants with a biocompatible low Young's modulus, Scr. Mater. 132 (2017) 34-38, https://doi.org/10.1016/j.scriptamat.2016.12.038.
- [21] S. Chen, G. Guillemot, C.-A. Gandin, Three-dimensional cellular automaton-finite element modeling of solidification grain structures for arc-welding processes, Acta Mater. 115 (2016) 448–467, https://doi.org/10.1016/j.actamat.2016.05.011.
- [22] Z. Sun, X. Tan, S.B. Tor, C.K. Chua, Simultaneously enhanced strength and ductility for 3D-printed stainless steel 316L by selective laser melting, NPG Asia Mater. 10 (2018) 127–136, https://doi.org/10.1038/s41427-018-0018-5.
- [23] C. Zhao, K. Fezzaa, R.W. Cunningham, H. Wen, F. De Carlo, L. Chen, A.D. Rollett, T. Sun, Real-time monitoring of laser powder bed fusion process using high-speed X-ray imaging and diffraction, Sci. Rep. 7 (2017), 3602, https://doi.org/10.1038/ s41598-017-03761-2.
- [24] U.F. Kocks, C. Tomé, H.-R. Wenk, Texture and Anisotropy: Preferred Orientations in Polycrystals and Their Effect on Material Properties, Cambridge University Press. 2000.
- [25] D.C. Hofmann, J. Kolodziejska, S. Roberts, R. Otis, R.P. Dillon, J.-O. Suh, Z.-K. Liu, J.-P. Borgonia, Compositionally graded metals: a new frontier of additive manufacturing, J. Mater. Res. 29 (2014) 1899–1910, https://doi.org/10.1557/ imr.2014.208.
- [26] D.C. Hofmann, S. Roberts, R. Otis, J. Kolodziejska, R.P. Dillon, J. Suh, A.A. Shapiro, Z.-K. Liu, J.-P. Borgonia, Developing gradient metal alloys through radial deposition additive manufacturing, Sci. Rep. 4 (2014) 1–8, https://doi.org/ 10.1038/srep05357.

- [27] H. Wu, G. Fan, An overview of tailoring strain delocalization for strength-ductility synergy, Prog. Mater. Sci. 113 (2020), 100675, https://doi.org/10.1016/j. pmateri 2020 100675
- [28] V.A. Popovich, E.V. Borisov, A.A. Popovich, V.Sh Suffiarov, D.V. Masaylo, L. Alzina, Functionally graded Inconel 718 processed by additive manufacturing: crystallographic texture, anisotropy of microstructure and mechanical properties, Mater. Des. 114 (2017) 441–449, https://doi.org/10.1016/j.matdes.2016.10.075.
- [29] E. Hernández-Nava, P. Mahoney, C.J. Smith, J. Donoghue, I. Todd, S. Tammas-Williams, Additive manufacturing titanium components with isotropic or graded properties by hybrid electron beam melting/hot isostatic pressing powder processing, Sci. Rep. 9 (2019) 1–11, https://doi.org/10.1038/s41598-019-40722.
- [30] F. Chen, J. Zabalza, P. Murray, S. Marshall, J. Yu, N. Gupta, Embedded product authentication codes in additive manufactured parts: Imaging and image processing for improved scan ability, Addit. Manuf. 35 (2020), 101319, https://doi.org/10.1016/j.addma.2020.101319.
- [31] X. Zhou, K. Li, D. Zhang, X. Liu, J. Ma, W. Liu, Z. Shen, Textures formed in a CoCrMo alloy by selective laser melting, J. Alloy. Compd. 631 (2015) 153–164, https://doi.org/10.1016/j.iailcom.2015.01.096.
- [32] L.L. Parimi, R.G. A, D. Clark, M.M. Attallah, Microstructural and texture development in direct laser fabricated IN718, Mater. Charact. 89 (2014) 102–111, https://doi.org/10.1016/j.matchar.2013.12.012.
- [33] Y. Lian, Z. Gan, C. Yu, D. Kats, W.K. Liu, G.J. Wagner, A cellular automaton finite volume method for microstructure evolution during additive manufacturing, Mater. Des. 169 (2019), 107672, https://doi.org/10.1016/j.matdes.2019.107672.
- [34] X. Wang, J.A. Muñiz-Lerma, M. Attarian Shandiz, O. Sanchez-Mata, M. Brochu, Crystallographic-orientation-dependent tensile behaviours of stainless steel 316L fabricated by laser powder bed fusion, Mater. Sci. Eng. A 766 (2019), 138395, https://doi.org/10.1016/j.msea.2019.138395.
- [35] X. Wang, J.A. Muñiz-Lerma, O. Sanchez-Mata, S.E. Atabay, M.A. Shandiz, M. Brochu, Single-crystalline-like stainless steel 316L with different geometries fabricated by laser powder bed fusion, Prog. Addit. Manuf. 5 (2020) 41–49, https://doi.org/10.1007/s40964-020-00123-9.
- [36] C. Körner, M. Ramsperger, C. Meid, D. Bürger, P. Wollgramm, M. Bartsch, G. Eggeler, Microstructure and mechanical properties of CMSX-4 single crystals prepared by additive manufacturing, Met. Mat. Trans. A 49 (2018) 3781–3792, https://doi.org/10.1007/s11661-018-4762-5.
- [37] G.L. Knapp, N. Raghavan, A. Plotkowski, T. DebRoy, Experiments and simulations on solidification microstructure for Inconel 718 in powder bed fusion electron beam additive manufacturing, Addit. Manuf. 25 (2019) 511–521, https://doi.org/ 10.1016/j.addma.2018.12.001.
- [38] L.C. Wei, L.E. Ehrlich, M.J. Powell-Palm, C. Montgomery, J. Beuth, J.A. Malen, Thermal conductivity of metal powders for powder bed additive manufacturing, Addit. Manuf. 21 (2018) 201–208, https://doi.org/10.1016/j.addma.2018.02.002.
- [39] A.T. Polonsky, W.C. Lenthe, M.P. Echlin, V. Livescu, G.T. Gray, T.M. Pollock, Solidification-driven orientation gradients in additively manufactured stainless steel, Acta Mater. 183 (2020) 249–260, https://doi.org/10.1016/j. actamat 2019 10 047